Laser & Photonics Reviews

LASER & PHOTONICS REVIEWS

www.lpr-journal.org

RESEARCH ARTICLE

All-Optical Circle Fitting via Vortex-Antivortex Convolution Merging Within a Single Metasurface

Haotian Zheng[1] | Haiyang Ren[1] | Pengcheng Huo[1,2] | Yanzeng Zhang[1] | Haocun Qi[1] | Yaqi Jin[1] | Le Tan[1] | Lizhi Fang[1] | Qingbin Fan[1] | Yan-qing Lu[1,2] | Ting Xu[1,2,3]

[1]National Laboratory of Solid-State Microstructures, College of Engineering and Applied Sciences, and Collaborative Innovation Center of Advanced Microstructures, Nanjing University, Nanjing, China | [2]Key Laboratory of Intelligent Optical Sensing and Manipulation, Nanjing University, Nanjing, China | [3]School of Materials Engineering, Jiangsu University of Technology, Changzhou, China

Correspondence: Pengcheng Huo (huopc@nju.edu.cn) | Yan-qing Lu (yqlu@nju.edu.cn) | Ting Xu (xuting@nju.edu.cn)

Received: 26 August 2025 | **Revised:** 28 December 2025 | **Accepted:** 14 January 2026

Keywords: circle fitting | metasurface | optical vortex

ABSTRACT

Circle fitting is a fundamental operation in recognition, localization, and measurement tasks across diverse scientific and technical domains. Traditionally, this process relies on image acquisition and subsequent digital processing, typically implemented via integrated electronic circuits. However, the inherent latency from sequential post-processing poses a significant challenge, particularly in applications that require real-time responsiveness or involve high-throughput data processing. Inspired by the Hough gradient method widely used in computer vision and leveraging the real-time, post-processing-free nature of optical computing, we propose an all-optical circle fitting technique based on a metasurface-integrated 4f spatial filtering system. A pair of optical vortex–antivortex kernels are compactly merged within a single dielectric metasurface, allowing simultaneous gradient extraction and intersection accumulation via passive optical convolution. The proposed framework demonstrates high robustness, accurately detecting circular features across a broad range of radii and structural imperfections. This work establishes a platform for integrated optical shape analysis and underscores the promise of metasurface-enabled optical computing in real-time machine vision and advanced metrology.

1 | Introduction

Circles are one of the most fundamental geometric shapes, appearing ubiquitously in natural systems, engineered structures, and scientific imagery. Accurate detection and fitting of circular features are thus essential for a broad range of localization and measurement tasks. To address this need, circle fitting has emerged as a foundational computational technique capable of both distinguishing circular patterns from input image and accurately locating centers, which has been widely applied in many fields including computer vision [1, 2], industrial inspection [3, 4], biomedical imaging [5, 6] and robotic navigation [7–9]. Conventionally, these operations are performed using digital algorithms implemented on electronic processors. However, in scenarios requiring real-time response or high data volumes, digital computing increasingly encounters limitations due to unavoidable latency introduced by sequential post-processing. In contrast, optical computing, which harnesses light to encode, transmit, and process information, enables instantaneous view-to-result computation, eliminating the need for post-processing and offering a promising solution for ultra-fast and low-latency tasks [10–18]. Embedding circle fitting algorithms within optical

Haotian Zheng and Haiyang Ren contributed equally to this work.

computing frameworks holds significant promise for enabling real-time geometric analysis.

In recent years, metasurface, a flat optical element composed of subwavelength nanostructures, has emerged as a powerful platform for precise manipulation of light at the nanoscale. Owing to their exceptional ability to freely tailor the phase, amplitude, and polarization of incident light, metasurfaces offer unprecedented flexibility in wavefront engineering, while maintaining ultrathin form factors and excellent integration compatibility [19–24]. These unique characteristics make metasurfaces highly attractive for a wide range of applications in flat optics and computational photonics. Notably, metasurface-based optical computing has enabled novel implementations of optical differentiator [25–31], optical accelerator [32, 33] and optical neural network [34–37]. While optical computing has achieved remarkable progress in various tasks, the experimental realization and practical deployment of high-precision optical circle fitting on integrated metasurface platforms remain largely unexplored. This is primarily due to the lack of a suitable optical computing architecture and algorithm capable of performing optical circle fitting without prior knowledge of geometric parameter and in the presence of substantial defects — let alone achieving high accuracy, precision, and robustness.

Here, we propose and experimentally demonstrate a high-precision and robust all-optical circle fitting technology based on a dielectric metasurface, which merging a pair of vortex-antivortex convolution kernels within a 4f spatial filtering system. By optically mimicking the Hough gradient method widely used in computer vision [38], our design enables real-time, accurate circle detection and localization. The experimental results demonstrate the proposed architecture's powerful capability in discriminating subtle shape differences, detecting circular features with defects, and achieving high-precision localization in practical scenarios, laying the groundwork for advanced optical computing in vision and metrology applications

2 | Results

2.1 | The Principle of Optical Circle Fitting

Inspired by the circle fitting process of the Hough gradient method widely used in computer vision, we construct an optical analogue for implementing all-optical high-precision circle fitting, named as the optical Hough gradient method (OHGM). The underlying principle is illustrated in Figure 1a and involves two main stages. The first stage applies a gradient operator to the input image to extract the gradient information of edges, represented as a gradient vector map (marked as red arrows in Figure 1a. In the second stage, these vectors are extended to find their intersections, and an accumulator is used to record the number of the vectors passing through each intersection point. A point with a count exceeding a predefined threshold is identified as the center of a circle. If no such point exists, the input pattern is classified as non-circular.

In the corresponding optical architecture, both processing stages of the circle fitting can be implemented via optical convolution operations. Figure 1b presents two typical optical convolution kernels used in our OHGM. One kernel, referred to as kernel U, features a vortex phase profile with a topological charge of $l = +1$ and a donut-shaped amplitude distribution. The other, denoted as kernel V, possesses an antivortex phase profile with a topological charge of $l = -1$ and incorporates a radial reverse operator consisting of concentric annular zones with alternating phase shifts of 0 and π. The vortex convolution kernel U is a continuous 2D gradient operator, which can construct a finer and faithful gradient vector map by sampling the intensity variations in all directions around a central point (see Section S1 for details).

The antivortex phase structure in the proposed kernel V plays a key role in realizing the optical intersection accumulator. The working principle is illustrated in the left panel of Figure 1c. During convolution, the input image slides over a fixed kernel; therefore, the azimuthal angle θ defined in the kernel's coordinate varies as the image moves, whereas the gradient vectors extracted from the circular boundary remain their orientation angle ψ unchanged. When the center of the input circle (marked as a red cross) is precisely aligned with the kernel center (denoted as the origin of the kernel coordinate system), the gradient vectors (red arrows) obtained from the circular boundary naturally point toward the kernel center. Here, the orientation of each gradient vector represents the phase of the local gradient field. Due to their uniform angular distribution, the vector sum of these gradients is close to zero.

However, by multiplying the gradient vector map with an antivortex phase kernel $exp(-i\theta)$, each gradient vector is rotated clockwise by its corresponding azimuthal angle θ, producing a rotated vector map (blue arrows). In the perfectly centered case, the azimuthal angle θ defined in the kernel coordinate coincides with the orientation angle ψ of the boundary gradients, enabling ideal alignment toward a common direction. Consequently, the vector sum becomes significantly enhanced, yielding a bright spot at the kernel center, which serves as an indicator of the circle center.

The superimposed reverse operator on the antivortex phase is also indispensable to further suppress the full-width at half-maximum (FWHM) of the center peak in circle fitting output, and enhance localization precision. As illustrated in the right panel of Figure 1c, when the circle center is slightly offset from the kernel center, the azimuthal angle θ no longer equals the gradient orientation angle ψ. As a result, the rotated gradient vectors are no longer perfectly aligned. Nevertheless, they still point roughly toward a similar direction (quasi-alignment), and thus their vector sum can remain relatively strong, producing an erroneously high response at off-center locations. To suppress such off-center responses and produce a sharper peak strictly at the true circle center, we introduce an additional radial reverse operator on top of the antivortex phase kernel. This modulation exhibits a radially periodic structure composed of alternating red (phase 0) and blue (phase π) concentric rings. Specifically, the blue rings are designed as reversal zones, where any gradient vector falling within these regions will undergo a directional flip, while the vectors falling within the red rings retain their original direction. This alternating modulation ensures that, when the input circle is slightly offset from the kernel center, a portion of the rotated vectors fall within the blue reversal zones are flipped (depicted as brown arrows in Figure 1c, thereby breaking the quasi-alignment of the gradient vectors and inducing destructive

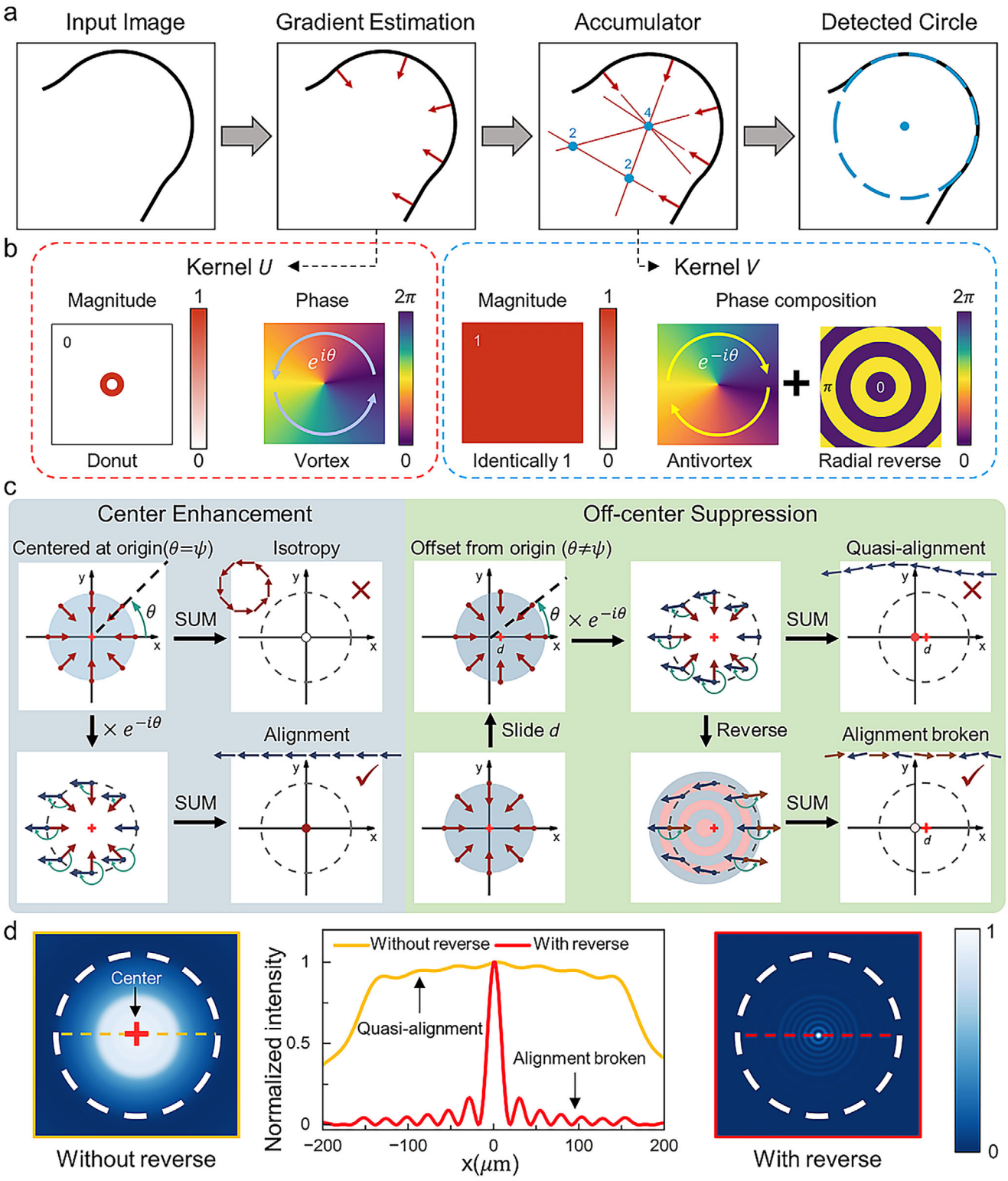

FIGURE 1 | The principle of optical circle fitting using OHGM. (a) The basic principle diagram of OHGM. (b) The two proposed optical vortex-antivortex kernels. Kernel *U* corresponds to gradient operator and kernel *V* corresponds to accumulator operator. (c) Principle of the kernel *V*. Kernel *V* is composited of an antivortex phase which can rotate gradient clockwise by its azimuthal angle θ and a reverse operator which can flip the gradient fall within the blue(π) ring. Left: Center enhancement achieved via the antivortex phase. Right: Off-center suppression enabled by a reverse operator superimposed on the antivortex kernel. (d) Enhancement in localization precision enabled by reverse operator. The profiles show intensity distributions along lines passing through the estimated circle centers.

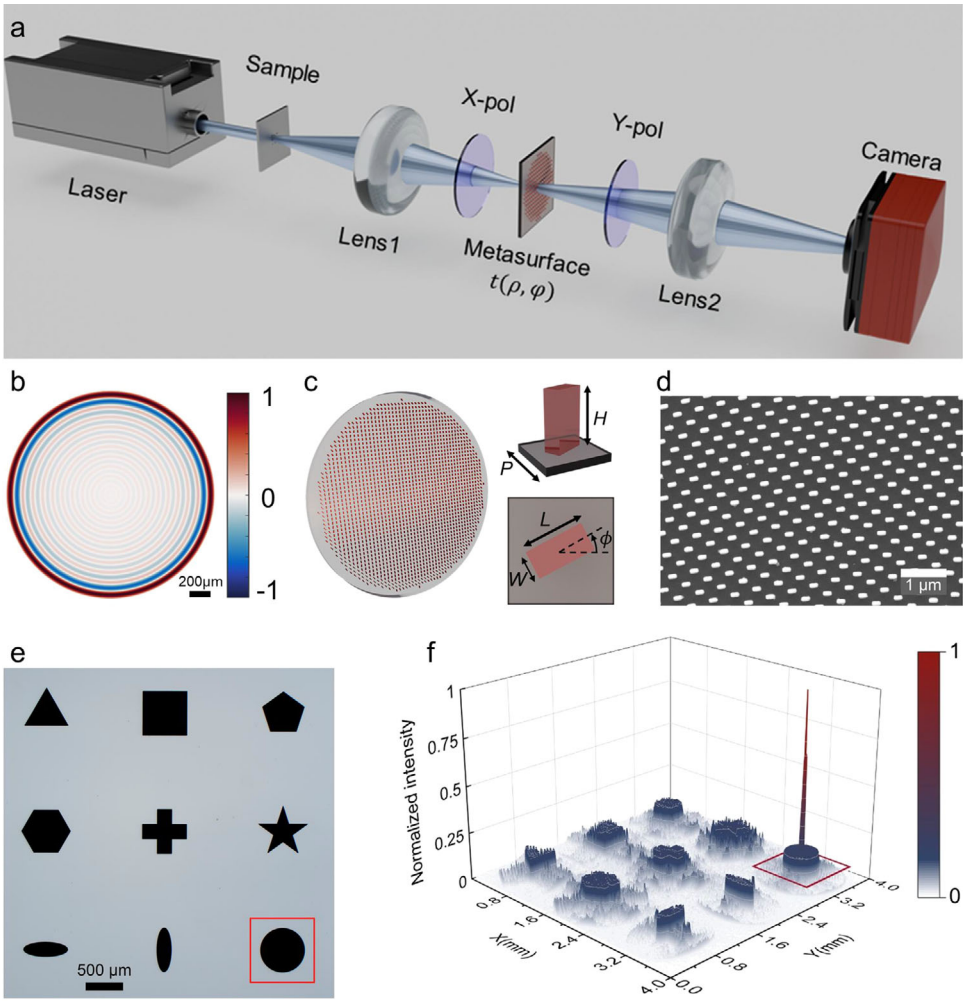

FIGURE 2 | Design and fabrication of metasurface device. (a) Experimental set up for circle fitting using the OHGM. (b) Illustration of the metasurface transmission function $t(\rho, \varphi)$. Scale bar: 200 μm. (c) Schematic of the designed dielectric metasurface. Inset: perspective view of a single unit cell. The parameters L, W, H, P and ϕ denote the nanorod length, width, height, square lattice constant, and rotation angle, respectively. (d) Top-view scanning electron microscope (SEM) images of the fabricated metasurface. Scalebar: 1 μm. (e) Fabricated test sample containing various geometric shapes. Scalebar: 500 μm. (f) Experimental demonstration of OHGM.

cancellation in their vector summation. Consequently, off-center responses are effectively suppressed, while all vectors contribute constructively at the correct center position to produce a sharply localized bright peak.

To demonstrate the enhancement in localization precision enabled by the reverse operator, we numerically simulated and compared the optical circle fitting performance with and without it, as shown in Figure 1d. An intensity profile was extracted along a line passing through the fitted circle center. The FWHM of the response obtained using the reverse is only 4.96% of that without it, indicating a more than 20-fold enhancement in the localization precision of optical circle fitting.

2.2 | Design and Fabrication of Metasurface

Figure 2a presents a schematic illustration of the optical setup for optical circle fitting using the OHGM. The core architecture is a standard 4f imaging system, with a metasurface device positioned at the Fourier plane of the system. According to the principle of spatial filtering [39], the output image under coherent illumination is the convolution result of the input light field and the system's coherent point spread function (cPSF). This cPSF can be approximated by the Fourier transform of the metasurface's transmission function $t(\rho, \varphi)$.

In our design, the cPSF is engineered as the convolution of two vortex-antivortex kernels, $U(r, \theta)$ and $V(r, \theta)$, as follows,

$$cPSF = U(r, \theta) \otimes V(r, \theta) = \mathcal{F}[t(\rho, \varphi)] \quad (1)$$

where (r, θ) and (ρ, φ) represent the polar coordinates in the spatial domain and the spatial frequency domain, respectively, and $\otimes$ denotes the convolution operation. According to the Fourier transform theory, the transmission function of the metasurface can be further derived as $t(\rho, \varphi) = u(\rho, \varphi) \times v(\rho, \varphi)$, where $u(\rho, \varphi) = \mathcal{F}^{-1}[U(r, \theta)]$ and $v(\rho, \varphi) = \mathcal{F}^{-1}[V(r, \theta)]$. Owing to the conservation of orbital angular momentum (OAM) under Fourier transform, u and v inherit the respective OAM values of the

convolution kernels U and V. This results in the merging of vortex and antivortex components within the metasurface, effectively canceling out their phase topological structures. Consequently, the resulting transmission function $t(\rho, \varphi)$ becomes radially symmetric and depends solely on the radial coordinate ρ, as shown in Figure 2b. In our implementation, $t(\rho)$ is designed as a real-valued binary-phase function, where positive values correspond to a phase of 0 and negative values correspond to a phase of π (see Section S3 for details).

Figure 2c shows the schematic of the proposed dielectric metasurface, which consists of silicon nitride rectangular nanorods with a long axis $L = 210$ nm, short axis $W = 100$ nm, and height $H = 600$ nm. The metasurface leverages linear cross-polarization modulation to realize the transmission function described in Figure 2b. The polarization response of a single nanorod rotated by an angle ϕ is described by the Jones matrix:

$$\begin{aligned} M &= R(-\phi)\begin{pmatrix} t_x & 0 \\ 0 & t_y \end{pmatrix} R(\phi) \\ &= \begin{pmatrix} t_x\cos^2\phi + t_y\sin^2\phi & (t_x - t_y)\sin\phi\cos\phi \\ (t_x - t_y)\sin\phi\cos\phi & t_x\sin^2\phi + t_y\cos^2\phi \end{pmatrix} \end{aligned} \tag{2}$$

where t_x and t_y are the complex transmission coefficients for linearly polarized light along the x and y directions, respectively. When x-polarized light $|H\rangle$ is incident on the metasurface, the y-polarized component $|V\rangle$ transmitted through a crossed polarizer can be analytically expressed as:

$$|out\rangle = \begin{pmatrix} 0 & 0 \\ 0 & 1 \end{pmatrix} M \ |H\rangle = (t_x - t_y)\ \sin\phi\cos\phi\ |V\rangle \tag{3}$$

Since identical nanorods are used throughout the metasurface, the transmission coefficients t_x and t_y can be treated as constants. By precisely adjusting the rotation angle Φ of each nanorod, the amplitude of the transmitted y-polarized light can be continuously modulated, while the phase is restricted to two discrete levels (0 or π), consistent with the binary-phase profile shown in Figure 2b. At the design wavelength of 450 nm, we select a square lattice constant $p = 400$ nm to ensure high polarization conversion efficiency and accurate amplitude modulation. Unlike conventional designs that rely on multiple discrete nanostructures, our approach employs a single nanorod geometry to achieve near-continuous amplitude modulation via rotation, simplifying fabrication and enhancing design flexibility (see Section S5 for details).

Figure 2d shows scanning electron microscope (SEM) images of the fabricated metasurface. The device was constructed from a 600 nm-thick silicon nitride film deposited on a transparent substrate. Using electron beam lithography (EBL) followed by inductively coupled plasma-reactive ion etching (ICP-RIE) technology, we fabricated a metasurface with a diameter of 2 mm. To evaluate the device's circle detection performance, a complementary test mask was fabricated via ultraviolet (UV) lithography and lift-off processes, as shown in Figure 2e. Each test pattern has a lateral size ranging from 500 to 800 μm. According to the principles of our proposed OHGM, circular input patterns should generate a distinct bright spot at the center in the output image. Figure 2f shows the experimental recognition results for a variety of input geometries, including triangles, squares, pentagons, circles, ellipses, crosses, and pentagrams. As observed, only the circular input results in a sharply focused intensity peak at its center, confirming the effectiveness of the metasurface-based OHGM in accurately identifying true circular features.

2.3 | Performance Evaluation of the Metasurface-Based OHGM

To assess the shape discrimination limits of the metasurface-based OHGM, we designed two additional test samples. The first sample comprises both circular and elliptical patterns, while the second includes circular shapes alongside regular polygons. A circle can be considered a special case of an ellipse where the major and minor axes are equal. As the axial ratio — defined as the ratio of the major axis to the minor axis — approaches unity, the ellipse increasingly approximates a circle. For the circle-vs.-ellipse discrimination experiment, we fabricated a series of test masks containing circular and elliptical patterns with axial ratios incremented in steps of 0.05, as illustrated in Figure 3a. The corresponding optical circle fitting results are shown in Figure 3b. To quantitatively evaluate detection performance, we introduce an accumulator score defined as the ratio of the total intensity between the nearest valleys surrounding the local peak region to the total intensity within the corresponding output area. This metric serves as a quantitative indicator to differentiate circular from non-circular patterns, with higher scores reflecting greater similarity to an ideal circle. Figure 3c depicts the accumulator score as a function of axial ratio. The experimental data demonstrate that the device can resolve ellipses with axial ratio differences as small as 0.05. Notably, it distinctly differentiates a perfect circle from an ellipse with an axial ratio of 1.05, showing a relative accumulator score difference of 9.8%.

Furthermore, a circle can be interpreted as a limiting case of a regular polygon with an infinite number of sides. As the polygon's side count increases, its shape progressively approximates a circle. To investigate OHGM's discrimination capability in this context, we fabricated a series of test masks featuring both circular and regular polygonal patterns, as shown in Figure 3d. The corresponding optical circle fitting results are presented in Figure 3e. With increasing side number, polygons more closely resemble circles, resulting in a gradual increase in the accumulator score (Figure 3f). Nonetheless, the device reliably distinguishes a perfect circle from a regular 16-gon, with the former exhibiting a relative accumulator score advantage of 8.2%. In addition to shape recognition, we also evaluated the localization precision of OHGM. Figure 3g (left) presents a magnified view of a selected circular pattern (highlighted in red) alongside its corresponding circle fitting output. The circle center (marked with a red cross) is calculated from the sample and compared with the experimentally observed bright spot. The intensity profile along orange dotted line is presented in the right panel of Figure 3g, where the experimental peak aligns closely with the calculated center position. This agreement confirms the high localization precision of the proposed OHGM.

In practical applications, circular features often vary in size and may be partially occluded or incomplete due to defects.

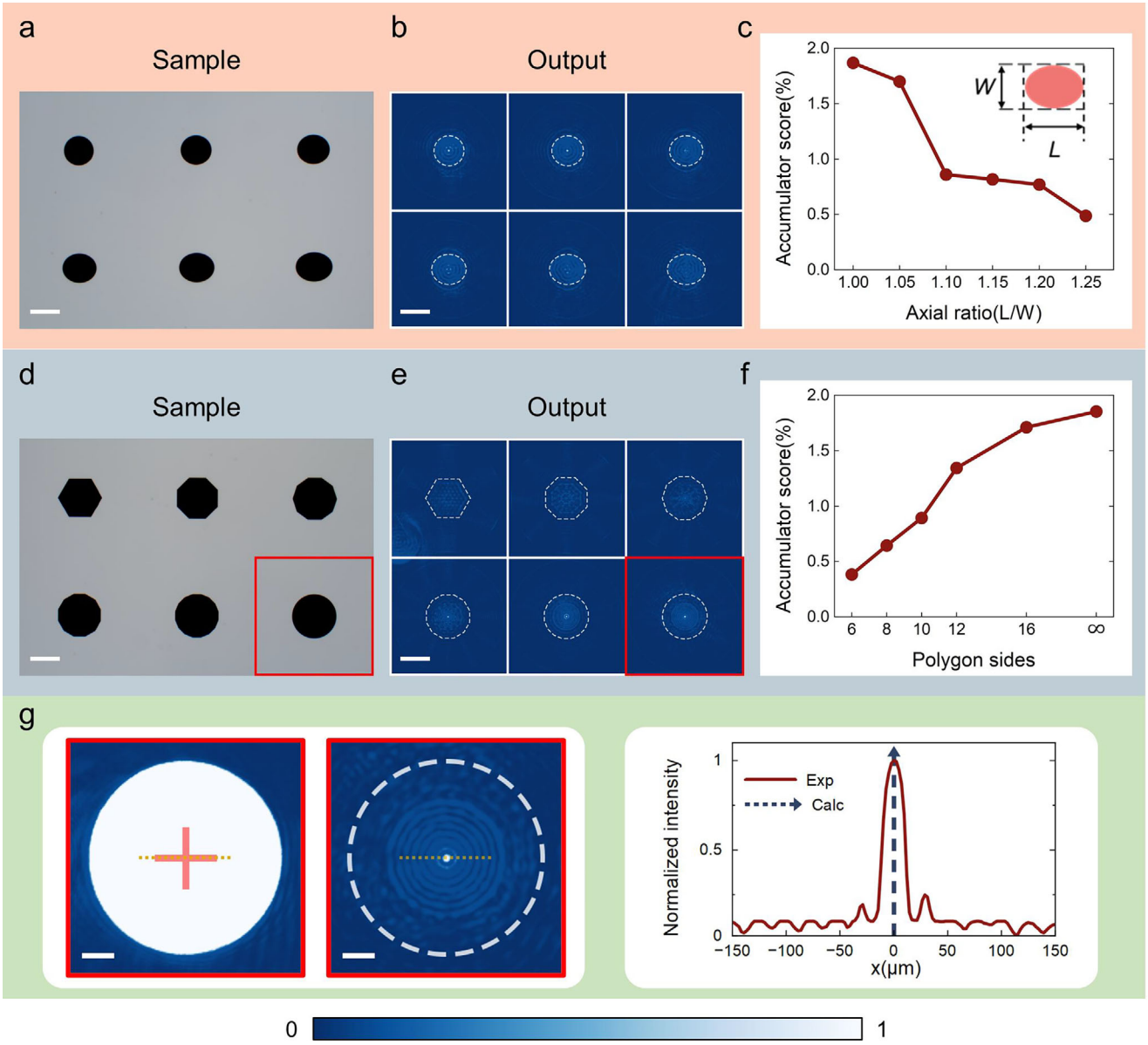

FIGURE 3 | Shape discrimination capability of OHGM. (a) Sample consist of circular and elliptical patterns with axial ratios incremented in steps of 0.05. (b) Circle fitting result obtained using OHGM for a. (c) Performance of OHGM in discriminating between circles and ellipses. (d) Sample consisting of circular and regular polygon patterns. (e) Circle fitting result for d. (f) Performance of OHGM in discriminating between circles and regular polygons. (g) Left: Magnified view of the sample and output from the red-highlighted region. Red cross marks the calculated circle center. Right: Intensity profile along the orange dotted line. Scale bars: 400 μm in a, b, d and e; 100 μm in g.

Therefore, a robust circle fitting approach must tolerate geometric variations including size changes and incomplete shapes such as semicircles and sectors. To evaluate OHGM's robustness under these conditions, we fabricated two sets of test masks: (i) circular patterns with varying radii (Figure 4a); and (ii) sector-shaped patterns with different central angles (Figure 4d). The corresponding experimental results are displayed in Figure 4b,e, respectively. As illustrated in Figure 4c, the accumulator score for circular patterns remains nearly constant across different radii, demonstrating the scale invariance of OHGM. Figure 4f plots the accumulator score as a function of sector central angle, showing a monotonic increase, which indicates that OHGM sensitively detects partially circular features. To further assess localization under partial input, Figure 4g (left) presents a zoomed-in view of a sector with a central angle of $3\pi/2$ (highlighted in red), together with its circle fitting output. The calculated circle center (red cross) closely matches the experimentally observed intensity peak (Figure 4g, right), demonstrating OHGM's high localization precision and robustness under incomplete geometric conditions.

2.4 | Verification of High-Precision Positioning Applications

The proposed OHGM-based optical circle fitting technique enables highly accurate detection of circular features, precise localization, and robust performance under geometric variations,

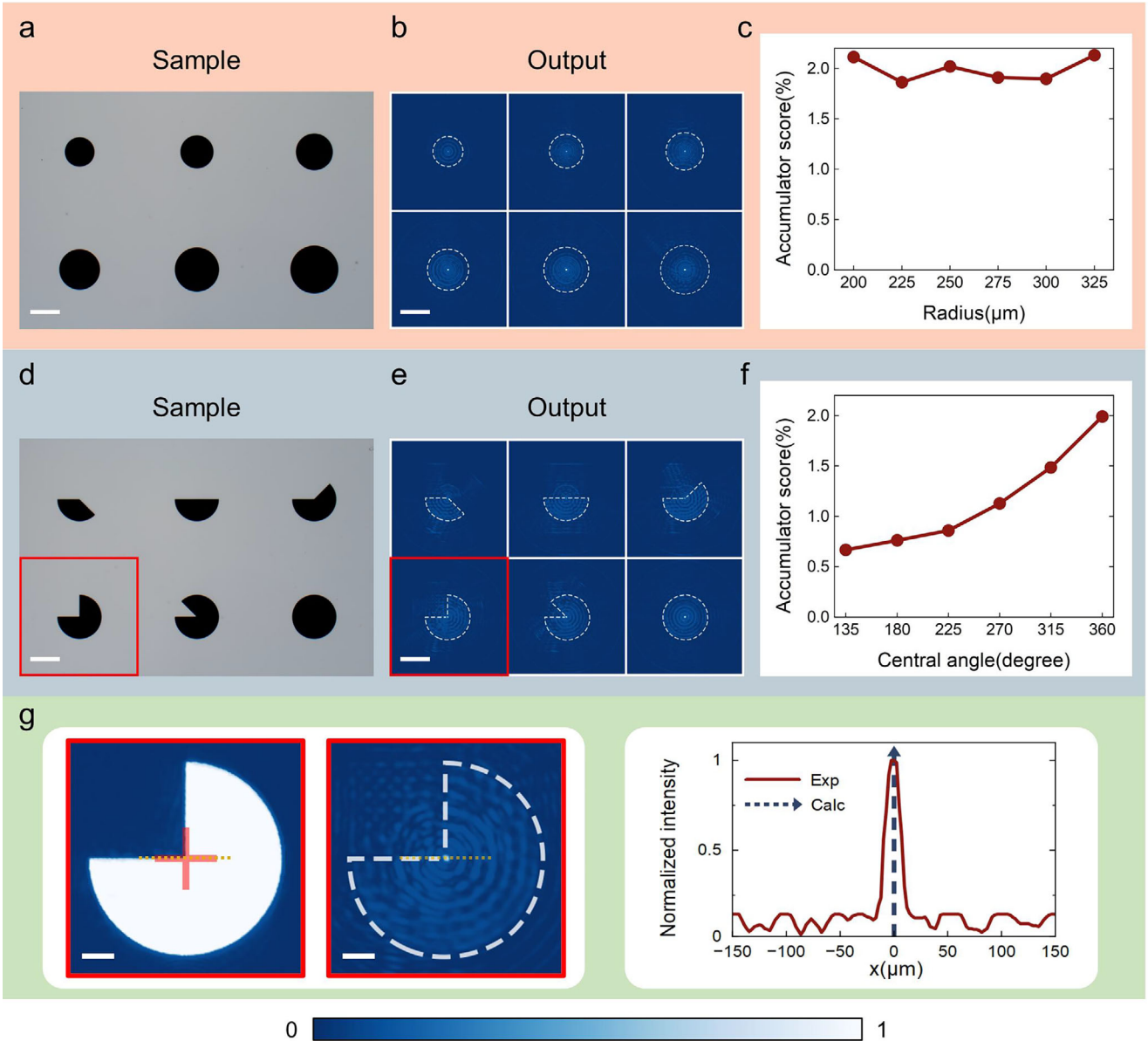

FIGURE 4 | Geometric robustness of OHGM. (a) Sample containing circle of various sizes. (b) Circle fitting result obtained using OHGM for a. (c) Performance of OHGM for circles of different sizes. (d) Sample consisting of sectors with different central angles. (e) Circle fitting result for d. (f) Performance of OHGM for sectors with different central angles. (g) Left: Magnified view of the sample and output from the red-highlighted region. Red cross marks the calculated circle center. Right: Intensity profile along the orange dotted line. Scale bars: 400 μm in a, b, d and e; 100 μm in g.

making it a promising tool for practical applications such as feature recognition, spatial positioning, and dimensional metrology. A representative application is the precise alignment of printed circuit boards (PCBs), which is essential for ensuring the accurate placement and reliable soldering of electronic components. While this task is conventionally addressed using computer vision algorithms, we demonstrate the potential of our metasurface-based approach for high-precision, all-optical alignment in PCB applications.

As illustrated in Figure 5a, we performed alignment experiments on a standard PCB sample. Four circular alignment holes, located in designated regions of the board (highlighted in orange in Figure 5a), were selected as test targets. The OHGM method was applied to determine their precise center positions. The captured optical image and the corresponding circle fitting results obtained via the metasurface are presented in Figure 5b,c, respectively. To assess the alignment accuracy, the calculated circle centers (indicated by red crosses) were superimposed on the output circle fitting image, as shown in Figure 5d. As evident, the bright intensity peaks generated by the metasurface coincide precisely with the true centers of the alignment holes, highlighting both the high localization precision and the practical utility of the OHGM technique in PCB positioning applications.

3 | Discussion

In summary, we propose and experimentally demonstrate a high-precision optical circle fitting framework using the proposed

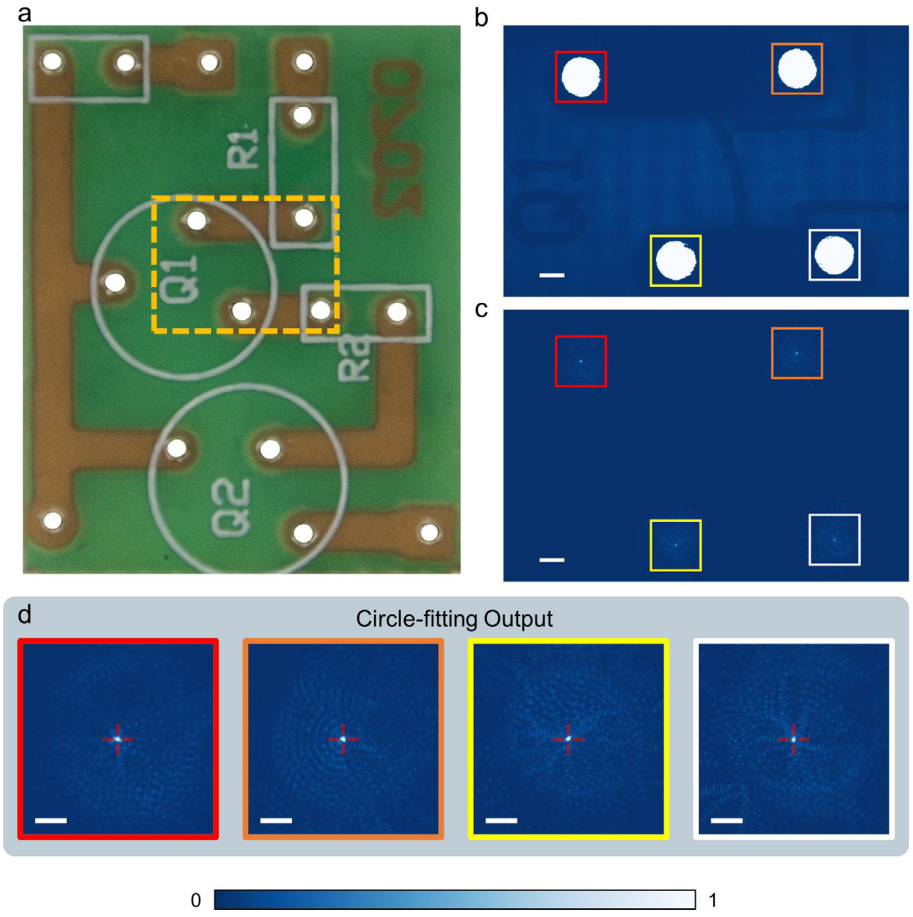

FIGURE 5 | (a) Schematic diagram of the PCB sample. (b) Optical image of specific regions on the PCB. (c) Circle fitting output obtained using OHGM. (d) Magnified view of the color-coded regions from the corresponding circle fitting output. Red crosses mark the calculated circle centers. Scale bars: 600 μm in b and c; 200 μm in d.

OHGM based on a metasurface-integrated 4f spatial filtering system. By introducing two specifically designed vortex-antivortex optical convolution kernels — a gradient operator and an intersection accumulator — OHGM enables accurate circle detection in a fully passive optical manner. Compared with traditional computer-based algorithms, OHGM leverages the inherent parallelism and ultrafast nature of optical computation to achieve circle fitting with minimal computational burden, suggesting broad potential for applications in machine vision, automated manufacturing, and optical information processing.

Beyond circle fitting, the presented framework is inherently extensible. By designing geometry-matched optical convolution kernels, it can be generalized to ellipse fitting and, more broadly, to the fitting and localization of arbitrary shapes. From a more practical perspective, future efforts can also be focused on scalable and cost-effective fabrication strategies to realize larger-aperture devices, enabling higher spatial resolution, improved fitting accuracy, and broader deployability in industrial production. With these advances, OHGM has the potential to serve as a versatile optical computing platform for high-throughput inspection and dimensional metrology, in-line quality control in automated manufacturing, robotic vision and alignment, semiconductor/display/panel defect inspection, and optical information processing and sensing.

4 | Methods

4.1 | Sample Fabrication

The metasurface is fabricated using electron-beam lithography (EBL) on a 600 nm thick silicon nitride film (SiNx) film with quartz substrate to pattern the specific arrays. First, a 600 nm-thick silicon nitride film is deposited on a fused silica substrate using plasma-enhanced chemical vapor deposition (PECVD). The gases required for the film deposition are SiH_4, NH_3, and N_2. Then, a 200 nm-thick electron beam resist (ARP6200) and a thin charge dissipation layer (ARPC5090) are spin-coated onto the SiNx film. Then, the sample is exposed through EBL, and the patterns are revealed after the development process. Afterward, a 30 nm thick Aluminum layer working as the hard etching mask is deposited on the sample by electron-beam evaporator, and the lift-off process is completed by immersing the sample in N-methyl-2-pyrrolidone (NMP) solution heated to 80°C for 10 min. Next, the patterns are transferred to SiNx film by inductively coupled plasma-reactive ion etching (ICP-RIE) technology, where CHF_3 and SF_6 are utilized during the etching process. Finally, the metasurface composed of silicon nitride nanopillars was obtained after complete removal of the aluminum mask using aluminum etchant (Sigma–Aldrich Aluminum Etchant Type A).

Author Contributions

P.H., Y.L., and T.X. conceived and supervised the project. H.Z. proposed the original idea and performed the theoretical verification, numerical simulations, sample design, and experiments. H.Z. and P.H. performed data analysis. H.Z. and H.R. contributed to the fabrication process. Y.Z., H.Q., Y.J., L.T., and L.F., provided useful discussions and comments. P.H. and H.Z. wrote the paper. All authors approved the manuscript.

Acknowledgements

We acknowledge support from the Key Research and Development Program of the Ministry of Science and Technology of China (2022YFA1205000 to T.X. and 2022YFA1207200 to P.H.), National Natural Science Foundation of China (12274217 to T.X. and 62105142 to P.H.), the Fundamental Research Funds for the Central Universities (021314380266 and KG202513). The authors acknowledge the technique support from the microfabrication center of the National Laboratory of Solid-State Microstructures.

Conflicts of Interest

The authors declare no conflicts of interest.

Data Availability Statement

All data needed to evaluate the conclusions in the paper are available in the manuscript or the Supplementary Materials.

References

1. S. Kumar, N. Ranganathan, and D. Goldgof, "Parallel Algorithms for Circle Detection in Images," *Pattern Recognition* 27 (1994): 1019–1028, https://doi.org/10.1016/0031-3203(94)90141-4.

2. L. Jiang, "A Fast and Accurate Circle Detection Algorithm Based on Random Sampling," *Future Generation Computer Systems* 123 (2021): 245–256, https://doi.org/10.1016/j.future.2021.05.010.

3. D. M. Tsai, "A Machine Vision Approach for Detecting and Inspecting Circular Parts," *The International Journal of Advanced Manufacturing Technology* 15 (1999): 217–221, https://doi.org/10.1007/s001700050059.

4. F. Mairesse, T. Sliwa, S. Binczak, and Y. Voisin, "Discrete Circles Measurement for Industrial Inspection," *Machine Vision Applications in Industrial Inspection XIV* (SPIE 2006), https://doi.org/10.1117/12.642326.

5. H. Pu, T. Peng, Z. Xu, et al., "A Morphological Indicator for Aortic Dissection: Fitting Circle of the Thoracic Aorta," *BMC Cardiovascular Disorders* 24 (2024): 461, https://doi.org/10.1186/s12872-024-04130-4.

6. S. Li, Z. Du, H. Yu, J. Zhao, and X. Han, "A Robust Circular Control Point Detector for bi-Planar Spine Surgery Navigation System," *IEEE Access* 6 (2018): 71084–71098, https://doi.org/10.1109/ACCESS.2018.2881446.

7. Y. Cui, X. Huang, Y. Wang, and R. Xiong, "Socially-Aware Multi-Agent Following With 2d Laser Scans via Deep Reinforcement Learning and Potential Field," in *2021 IEEE International Conference on Real-time Computing and Robotics (RCAR)* (IEEE, 2021), https://doi.org/10.1109/RCAR52367.2021.9517362.

8. P. Pásztó and P. Hubinský, "Mobile Robot Navigation Based on Circle Recognition," *J Electr Eng* 64 (2013): 84.

9. Y. Mochizuki, A. Imiya, and A. Torii, "Circle-Marker Detection Method for Omnidirectional Images and Its Application to Robot Positioning," in 2007 IEEE 11th International Conference on Computer Vision (ICCV) (IEEE, 2007), https://doi.org/10.1109/ICCV.2007.4409209.

10. N. C. Harris, G. R. Steinbrecher, M. Prabhu, et al., "Quantum Transport Simulations in a Programmable Nanophotonic Processor," *Nature Photonics* 11 (2017): 447–452, https://doi.org/10.1038/nphoton.2017.95.

11. J. Wang, S. Paesani, Y. Ding, et al., "Multidimensional Quantum Entanglement With Large-Scale Integrated Optics," *Science* 360 (2018): 285–291, https://doi.org/10.1126/science.aar7053.

12. J. Feldmann, N. Youngblood, M. Karpov, et al., "Parallel Convolutional Processing Using an Integrated Photonic Tensor Core," *Nature* 589 (2021): 52–58, https://doi.org/10.1038/s41586-020-03070-1.

13. P. L. McMahon, "The Physics of Optical Computing," *Nature Reviews Physics* 5 (2023): 717–734, https://doi.org/10.1038/s42254-023-00645-5.

14. N. Mohammadi Estakhri, B. Edwards, and N. Engheta, "Inverse-Designed Metastructures That Solve Equations," *Science* 363 (2019): 1333–1338, https://doi.org/10.1126/science.aaw2498.

15. X. Qiu, D. Zhang, W. Zhang, and L. Chen, "Structured-Pump-Enabled Quantum Pattern Recognition," *Physical Review Letters* 122 (2019): 123901, https://doi.org/10.1103/PhysRevLett.122.123901.

16. X. Xu, M. Tan, B. Corcoran, et al., "11 TOPS Photonic Convolutional Accelerator for Optical Neural Networks," *Nature* 589 (2021): 44–51, https://doi.org/10.1038/s41586-020-03063-0.

17. H. H. Zhu, J. Zou, H. Zhang, et al., "Space-Efficient Optical Computing With an Integrated Chip Diffractive Neural Network," *Nature Communications* 13 (2022): 1044, https://doi.org/10.1038/s41467-022-28702-0.

18. R. Hamerly, L. Bernstein, A. Sludds, M. Soljačić, and D. Englund, "Large-Scale Optical Neural Networks Based on Photoelectric Multiplication," *Physical Review X* 9 (2019): 021032.

19. N. Yu, P. Genevet, M. A. Kats, et al., "Light Propagation with Phase Discontinuities: Generalized Laws of Reflection and Refraction," *Science* 334 (2011): 333–337, https://doi.org/10.1126/science.1210713.

20. P. Huo, W. Chen, Z. Zhang, et al., "Observation of Spatiotemporal Optical Vortices Enabled by Symmetry-Breaking Slanted Nanograting," *Nature Communications* 15 (2024): 3055, https://doi.org/10.1038/s41467-024-47475-2.

21. P. Huo, M. Song, W. Zhu, et al., "Photorealistic Full-Color Nanopainting Enabled by a Low-Loss Metasurface," *Optica* 7 (2020): 1171–1172, https://doi.org/10.1364/OPTICA.403092.

22. J. Yao, F. Lai, Y. Fan, et al., "Nonlocal Meta-Lens With Huygens' Bound States in the Continuum," *Nature Communications* 15 (2024): 6543, https://doi.org/10.1038/s41467-024-50965-y.

23. M. Pu, X. Li, X. Ma, et al., "Catenary Optics for Achromatic Generation of Perfect Optical Angular Momentum," *Science Advances* 1 (2015): 1500396, https://doi.org/10.1126/sciadv.1500396.

24. G. Zheng, H. Mühlenbernd, M. Kenney, G. Li, T. Zentgraf, and S. Zhang, "Metasurface Holograms Reaching 80% Efficiency," *Nature Nanotechnology* 10 (2015): 308–312, https://doi.org/10.1038/nnano.2015.2.

25. P. Huo, C. Zhang, W. Zhu, et al., "Photonic Spin-Multiplexing Metasurface for Switchable Spiral Phase Contrast Imaging," *Nano Letters* 20 (2020): 2791–2798, https://doi.org/10.1021/acs.nanolett.0c00471.

26. A. Ji, J.-H. Song, Q. Li, et al., "Quantitative Phase Contrast Imaging With a Nonlocal Angle-Selective Metasurface," *Nature Communications* 13 (2022): 7848, https://doi.org/10.1038/s41467-022-34197-6.

27. Y. Kim, G. Y. Lee, J. Sung, J. Jang, and B. Lee, "Spiral Metalens for Phase Contrast Imaging," *Advanced Functional Materials* 32 (2022): 2106050, https://doi.org/10.1002/adfm.202106050.

28. Y. Zhang, P. Lin, P. Huo, et al., "Dielectric Metasurface for Synchronously Spiral Phase Contrast and Bright-field Imaging," *Nano Letters* 23 (2023): 2991–2997, https://doi.org/10.1021/acs.nanolett.3c00388.

29. P. Huo, L. Tan, Y. Jin, et al., "Broadband and Parallel Multiple-Order Optical Spatial Differentiation Enabled by Bessel Vortex Modulated Metalens," *Nature Communications* 15 (2024): 9045, https://doi.org/10.1038/s41467-024-53463-3.

30. Y. Zhou, H. Zheng, I. I. Kravchenko, and J. Valentine, "Flat Optics for Image Differentiation," *Nature Photonics* 14 (2020): 316–323, https://doi.org/10.1038/s41566-020-0591-3.

31. X. Bi, X. Wu, X. Fan, et al., "Concurrent Image Differentiation and Integration Processings Enabled By Polarization-Multiplexed Metasurface," *Laser & Photonics Reviews* 19 (2025): 2400718, https://doi.org/10.1002/lpor.202400718.

32. H. Zheng, Q. Liu, Y. Zhou, I. I. Kravchenko, Y. Huo, and J. Valentine, "Meta-Optic Accelerators for Object Classifiers," *Science Advances* 8 (2022): abo6410, https://doi.org/10.1126/sciadv.abo6410.

33. M. Luo, T. Xu, S. Xiao, H. K. Tsang, C. Shu, and C. Huang, "Meta-Optics Based Parallel Convolutional Processing for Neural Network Accelerator," *Laser & Photonics Reviews* 18 (2024): 2300984, https://doi.org/10.1002/lpor.202300984.

34. C. Wu, H. Yu, S. Lee, R. Peng, I. Takeuchi, and M. Li, "Programmable Phase-change Metasurfaces on Waveguides for Multimode Photonic Convolutional Neural Network," *Nature Communications* 12 (2021): 96, https://doi.org/10.1038/s41467-020-20365-z.

35. C. Liu, Q. Ma, Z. J. Luo, et al., "A Programmable Diffractive Deep Neural Network Based on a Digital-Coding Metasurface Array," *Nature Electronics* 5 (2022): 113–122, https://doi.org/10.1038/s41928-022-00719-9.

36. X. Luo, Y. Hu, X. Ou, et al., "Metasurface-Enabled on-Chip Multiplexed Diffractive Neural Networks in the Visible," *Light: Science & Applications* 11 (2022): 158, https://doi.org/10.1038/s41377-022-00844-2.

37. J. Peng, L. Fang, M. Gu, and Q. Zhang, "Dynamically Reconfigurable All-Optical Neural Network Based on a Hybrid Graphene Metasurface Array," *Optics Continuum* 3 (2024): 704–713, https://doi.org/10.1364/OPTCON.511737.

38. P. Kierkegaard, "A Method for Detection of Circular Arcs Based on the Hough Transform," *Machine Vision and Applications* 5 (1992): 249–263, https://doi.org/10.1007/BF01212714.

39. Y. Chen, "4f-Type Optical System for Matrix Multiplication," *Optical Engineering* 32 (1993): 77–79, https://doi.org/10.1117/12.60078.

Supporting Information

Additional supporting information can be found online in the Supporting Information section.

Supporting File: lpor70917-sup-0001-SuppMat.pdf.